DOI: 10.1002/ejic.200800675

Mesoporous Carbon Materials with Ultra-Thin Pore Walls and Highly Dispersed Nickel Nanoparticles

Pasquale F. Fulvio,[a] Chengdu Liang,[b] Sheng Dai,[b] and Mietek Jaroniec*[a]

Keywords: Mesoporous carbon / Nickel / Nanostructures / Mesoporous materials

Mesoporous carbon materials with ultra-thin carbon pore walls and highly dispersed Ni nanoparticles have been successfully prepared by using two different SBA-15 silicas as hard templates and 2,3-dihydroxynaphthalene (DHN) as a carbon precursor. The nickel precursor was a concentrated nickel nitrate hexahydrate [$Ni(NO_3)_2 \cdot 6H_2O$] solution in 2-propanol, which was added to the carbon–silica nanocomposite prior to thermal treatment. The samples studied were analyzed by thermogravimetry (TG), nitrogen adsorption at –196 °C, powder X-ray diffraction (XRD), Raman spectroscopy, scanning and transmission electron microscopy (STEM), and in situ electron diffraction X-ray spectroscopy (EDX). While TG analysis revealed carbon contents lower than 30 wt.-%, nitrogen adsorption provided information about the homogeneity of the carbon thin film deposited onto the mesopore walls of the ordered silica templates SBA-15. The templates, carbon–silica nanocomposites, and carbon inverse replicas with nickel nanoparticles exhibit uniform pores, high surface areas, and large pore volumes. Partially graphitic carbon was identified by the presence of a characteristic G band in the Raman spectra, whereas the diffraction peak attributed to the stacking of graphene planes was not observed by powder XRD. The presence of ordered domains in the carbon materials studied was confirmed by small angle XRD and STEM imaging. In addition, the STEM images revealed that the nickel nanoparticles are uniform in size, ca. 3 nm, and are homogeneously dispersed on the tubular carbon walls. A few larger clusters of nickel, ca. 60 nm, present on the external surface, were identified by powder XRD as metallic Ni. The in situ EDX revealed that the small nanoparticles are largely composed of Ni with traces of NiO. Similar nanoparticle dispersions have been reported only for Ni-containing multiwalled carbon nanotubes (CNTs), whereas previously reported ordered mesoporous carbon materials, CMK-3, possess larger Ni/NiO nanoparticles.

Introduction

Ordered mesoporous carbons (OMCs) have been successfully synthesized by using the confined pore geometries of ordered mesoporous silicas (OMSs) as hard templates. Some of the most commonly used OMS templates have been the MCM-48,[1] SBA-15, and SBA-16[2] materials. After filling the template pores with a carbon precursor, followed by carbonization and etching of the silica, stable inverse carbon replicas have been obtained. Among the aforementioned silica templates, SBA-15 has been largely used to prepare two types of carbon nanostructures, namely CMK-3[3] and CMK-5.[4,5] The SBA-15 silica consists of 2D hexagonally ordered cylindrical mesopores (*P6mm* symmetry) and is similar to its counterpart material MCM-41. SBA-15 is even more popular because of the availability and low cost of the triblock copolymer poly(ethylene oxide)–poly(propylene oxide)–poly(ethylene oxide) (PEO–PPO–PEO) used for its synthesis. Further, favorable interactions between the hydrophilic moieties of the triblock copolymer and the silica species allow the former to penetrate the silica pore walls, which leads to the formation of randomly distributed interconnecting small pores between ordered mesopores; consequently, SBA-15 is a 3D network of micropores and ordered mesopores.[6] By completely filling the ordered mesopores and interconnecting pores of SBA-15 with a carbon precursor, followed by carbonization and silica dissolution, a stable 3D structure of interconnected carbon rods can be obtained, which is known as CMK-3, whereas an incomplete filling of the ordered mesopores with the same precursor can lead to a stable structure of interconnected nanopipes known as CMK-5. In contrast, the OMSs prepared by using cationic alkylammonium surfactants, such as MCM-41 and MCM-48, do not possess small pores interconnecting the ordered mesopores, and the resulting carbon materials are disordered as in the case of MCM-41 or they are not true inverse replicas of MCM-48 because of a structure change.[7] The aforementioned change is due to a shift in the 3D cubic bicontinuous structure of the resulting carbon replica.

[a] Department of Chemistry, Kent State University, Kent, OH 44242, USA
Fax: +1-330-672 3816
E-mail: jaroniec@kent.edu
[b] Chemical Sciences Division and Center for Nanophase Materials Science, Oak Ridge National Laboratory, Oak Ridge, TN 37831, USA

Supporting information for this article is available on the WWW under http://www.eurjic.org or from the author.

While significant progress has been made towards the synthesis of the CMK-3 carbon materials with graphitic domains,[8–10] its particle morphology,[11,12] the incorporation of oxide[13–19] and metallic[20–22] nanoparticles, and the preparation of films,[23] the CMK-5 type of carbon materials have been less explored. One possible reason for this is the difficulty of finding suitable precursors that permit strict control of the pore wall thickness in order to obtain stable carbon replicas with graphitic pore walls similar to those in multiwall carbon nanotubes (CNTs). There are reports showing the possibility of preparing CMK-5 with controlled pore wall thickness by using different methods of polymerization of furfuryl alcohol[5,24,25] and ferrocene,[26] employed as carbon precursors. There are a few reports on the incorporation of highly dispersed nanoparticles of platinum[4,26] and cobalt[25] into CMK-5 in order to enhance its electrochemical and catalytic properties; in the case of cobalt-containing CMK-5, magnetic properties are also added. It has been shown that in the nanocasting synthesis of CMK-5 with furfuryl alcohol together with cobalt, iron, and nickel salts,[25] only the former afforded materials with carbon nanopipes. In the case of iron and nickel, only CMK-3 (rod-type structure) carbon materials have been reported.

A major step in the preparation of tubular carbon materials has been made by chemical vapor deposition (CVD) of acetylene in the MCM-48 channels.[27] Using this route, relatively stable carbon inverse replicas with ultra-thin pore walls have been obtained. Furthermore, the use of phenolic resins as carbon precursors afforded stable carbon thin films as inverse replicas of silica colloidal crystals.[28] In the case of SBA-15, stable ultra-thin carbon films have been reported for carbon–silica nanocomposites only.[29] An aromatic carbon precursor, 2,3-dihydroxynaphthalene (DHN), which reacts with silanols present on the silica surface, was used to form homogeneous ultra-thin carbon films, but they were unstable after silica dissolution. These carbon films obtained by carbonization of DHN attached to the siliceous pore walls were hydrophobic and electrically conductive as graphitic carbon materials.[29] Despite the lower molecular weight of DHN than that of the mesophase pitch molecules and phenolic resins, the ability of DHN to form chemical bonds with the silica surface[29–31] as well as its easy graphitization make this precursor attractive for further investigations.

In this work, two different SBA-15 samples were used as hard templates to attach DHN (carbon precursor) and to incorporate the nickel precursor from concentrated nickel nitrate alcohol solutions for the preparation of SBA-15 carbon–nickel and mesoporous carbon (MC) nickel nanocomposites with ultra-thin pore walls and magnetic properties. Nitrogen adsorption and powder XRD show that the resulting carbon materials are stable after dissolution of the silica template and that their adsorption and structural properties are affected by the properties of the SBA-15 templates. These carbon materials exhibit high surface areas, large pore volumes and mesopore widths that are comparable to those of the CMK-3 carbon materials, whereas the film thickness was estimated to be ca. 0.5–1.5 nm. HRTEM reveals that the resulting nickel nanoparticles are uniform in size (ca. 3 nm) and are homogeneously dispersed within the carbon-coated silica and carbon nanopipes. In situ EDX reveals that these nanoparticles are composed of Ni and NiO. These results differ from previous reports on CMK-3 and CMK-5 materials prepared by using much lower metal content, for which large particle clusters were almost exclusively observed.[19,25] The Raman spectra for these materials show distinct bands attributed to graphitic carbon, whereas the powder XRD patterns do not exhibit the characteristic reflection attributed to the stacking of graphene planes. Similar distributions of magnetic Ni nanoparticles have only been reported for multiwalled CNTs,[32] which suggest some similarity between both types of materials. Furthermore, it was shown earlier that the presence of dispersed Ni and NiO nanoparticles in activated carbon materials and CMK-3 had a pronounced effect on the properties as potential supercapacitors.[17,19,33] Nitrogen adsorption isotherms show accessible porosity of the nickel-containing mesoporous silica–carbon and carbon materials, which makes these materials promising for applications in sensing devices[34,35] and fuel cells.[36,37]

Results and Discussion

The small angle XRD patterns for the SBA-15 and SBA-15$^{\#}$ silica templates, hydrothermally treated at 100 and 140 °C, respectively (Figure 1A), exhibit at least five reflections (peaks), which indicate the highly ordered nature of these samples. These peaks are assigned according to the *P6mm* symmetry, characteristic for this type of materials, with the (100) Bragg reflection as the most intense peak. The d_{100} spacing for these silica samples is ca. 9.5 nm, which results in a unit cell value larger than 10.9 nm (Table 1). Analogous XRD patterns were obtained for the carbon-coated silicas [Figure S1(A) in the Supporting Information] and Ni-containing nanocomposites (Figure 1B), which are also assigned according to the *P6mm* symmetry. A comparison of the d_{100} spacing values for nanocomposites shows that these values are slightly smaller than those for the SBA-15 templates. The same trend is observed for the unit cell parameters listed in Table 1, which indicates structural shrinkage of these materials after film casting and thermal treatment at 800 °C. In general, the latter parameter decreases by ca. 10–12% for the samples prepared with the SBA-15 template, whereas a smaller decrease is observed for the SBA-15$^{\#}$ material (ca. 7%), which results from its better thermal stability.

After removal of the silica template, the small angle XRD patterns for the MC-Ni and MC$^{\#}$–Ni materials (Figure 1C) show a shoulder, which makes it impossible to assign a particular symmetry and comment on the structural ordering. A similar spectrum to that of MC$^{\#}$–Ni is obtained for MC$^{\#}$ [Figure S1(B) in the Supporting Information], whereas no peaks are found for MC [Figure S1(B) in the Supporting Information]. Nevertheless, by assuming the

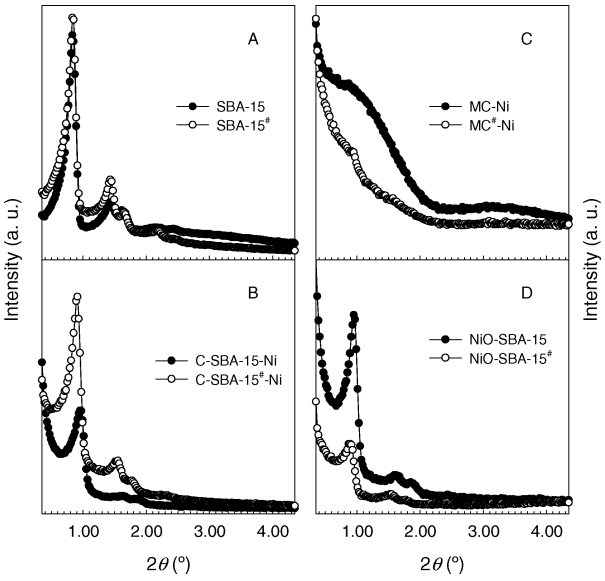

Figure 1. Small angle powder XRD patterns for (A) SBA-15, (B) carbon-SBA-15, (C) Ni-containing mesoporous carbon materials and (D) NiO–silica nanocomposites.

Table 1. Parameters obtained from small angle XRD and nitrogen adsorption at –196 °C for SBA-15, the nanocomposites and the MC samples studied.

Sample	a (nm)[a]	S_{BET} ($m^2 g^{-1}$)[b]	V_{SP} ($cm^3 g^{-1}$)[c]	w_{KJS} (nm) [d]	V_{mi} ($cm^3 g^{-1}$)[e]
SBA-15	10.95	960	1.41	9.74	0.10
SBA-15#	10.97	600	1.28	10.22	0.00
C–SBA-15–Ni	9.63	435	0.45	1.91 (7.54)	0.09
C–SBA-15#–Ni	10.21	290	0.46	8.30	0.04
MC–Ni	9.13	520	0.47	2.38 (3.77)	0.12
MC#–Ni	9.91	790	0.86	4.73	0.16
NiO–SBA-15	9.72	380	0.58	8.11	0.03
NiO–SBA-15#	10.27	230	0.47	9.75	0.01
C–SBA-15	9.77	540	0.64	7.66	0.08
C–SBA-15#	10.25	530	0.89	8.68	0.08
MC	–	780	0.60	6.43	0.24
MC#[f]	10.07	–	–	–	–

[a] Unit cell parameter. [b] Specific surface area calculated in a relative pressure range of 0.05–0.2. [c] Single-point pore volume calculated from the adsorption isotherms at a relative pressure of 0.98. [d] Pore width calculated with the improved KJS method; values in parentheses refer to the largest pores observed on PSDs and not to the maxima of PSDs. [e] Micropore volume obtained by integrating the PSD curves for pores up to 3 nm. [f] Adsorption parameters were not evaluated for MC# because of the small amount of the sample.

P6mm symmetry for the aforementioned carbon materials, the unit cell parameters calculated with the most intensive reflection peaks found by deconvolution of the observed shoulders are slightly smaller (about 0.5 nm) than those for the corresponding silica nanocomposites, possibly because of the additional shrinkage or partial collapse of the carbon framework after the dissolution of the template.

Nitrogen adsorption isotherms at –196 °C for SBA-15 and the Ni-containing materials are shown in Figure 2. Adsorption parameters such as the BET surface area, the pore volume, and pore width are listed in Table 1. These isotherms are presented by plotting the relative adsorption (=amount adsorbed divided by the BET monolayer capacity) vs. the relative pressure, which facilities comparison of isotherms for different materials. For SBA-15 and SBA-15# [Figure 2(a) and Figure 2(b), respectively] the adsorption isotherms are of type IV with steep capillary condensation steps and characteristic hysteresis loops for large and uniform cylindrical mesopores.

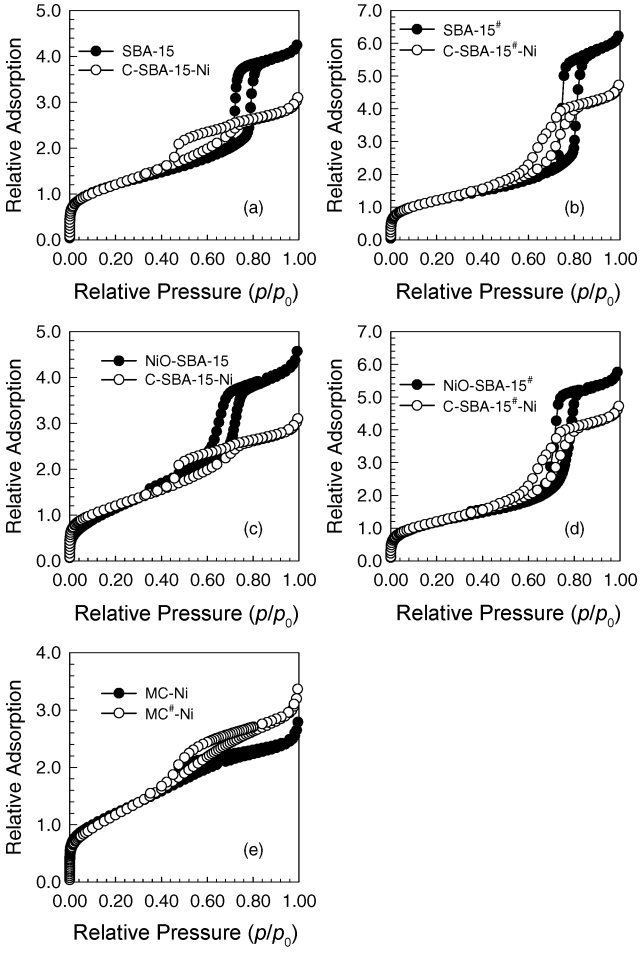

Figure 2. Nitrogen adsorption isotherms at –196 °C for (a) SBA-15 and C–SBA-15–Ni, (b) SBA-15# and C–SBA-15#–Ni, carbon-silica-nickel and silica-nickel oxide nanocomposites: (c) NiO–SBA-15 and (d) NiO–SBA-15#, and carbon-nickel composites: (e) MC–Ni and MC#–Ni. The adsorption isotherms are presented by plotting relative adsorption vs. relative pressure.

Both templates have high specific surface areas, 960 and 600 m^2/g for the SBA-15 and SBA-15# samples, respectively; a higher surface area (by about 62%) is obtained for the former sample, which was hydrothermally treated at a lower temperature, 100 °C vs. 140 °C. The total pore volume is also larger for the SBA-15 sample. The PSD (pore size distribution) curves (shown in Figure 3) for these samples reveal slightly larger mesopores (about 10.2 nm) for SBA-15#. The volume of complementary pores, pores below 3 nm, is larger for SBA-15, whereas SBA-15# is entirely a mesoporous sample. These data are in good agreement with previous findings for the SBA-15 materials hydrother-

mally treated at 140 °C; high-temperature hydrothermal treatment causes an increase in the size of interconnecting pores.[38]

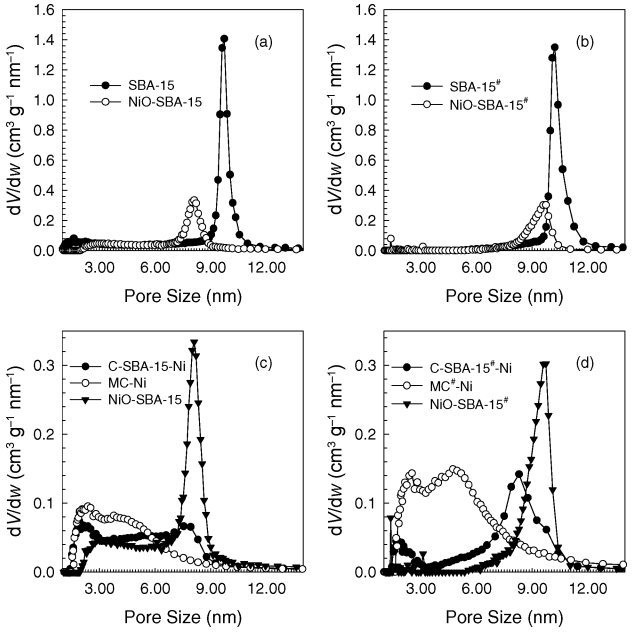

Figure 3. The PSD curves calculated according to the improved KJS method for the SBA-15 templates and Ni-containing nanocomposites.

Adsorption isotherms for carbon–silica–nickel nanocomposites are also type IV, as shown in Figure 2(a) for C–SBA-15–Ni and in Figure 2(b) for C–SBA-15#–Ni; a narrower hysteresis loop for the latter sample and a delayed desorption for the former can be seen. Similar isotherms are obtained for the C–SBA-15 and C–SBA-15# materials [see Figure S2(a) and (b) in the Supporting Information, respectively]. As can be seen from Figure 2, a steeper capillary condensation step and a two-step desorption branch is observed for C-SBA-15. Thus, despite the use of a carbon precursor that tends to form an ultra-thin carbon film on the SBA-15 pore walls, some pores of the template are partially blocked by carbon. A similar effect is observed for C–SBA-15–Ni, but in this case, Ni nanoparticles could also be responsible for the partial pore blocking. Furthermore, the capillary condensation steps for nanocomposites are shifted to lower relative pressures as a result of the decrease in the pore width because of the introduction of carbon and nickel into the mesopores of SBA-15. In general, the Ni-containing materials also exhibit lower surface areas (about 20–56%) than those for the corresponding Ni-free counterparts. The single-point pore volumes for C–SBA-15–Ni and C–SBA-15#–Ni are also significantly lower (see Table 1).

To estimate the decrease in the pore width upon formation of the carbon film at 800 °C, the carbon was removed by calcination at 500 °C [see isotherms in Figure 2(c) and (d)]. As can be seen from these figures, nitrogen adsorption isotherms for both the NiO–SBA-15 and NiO–SBA-15# samples show capillary condensation steps at slightly higher relative pressures than those for the corresponding carbon nanocomposites, which indicates that the pore widths of the former are larger (see Figure 3). Thus, the thickness of the carbon films could be estimated by the difference between the pore widths of the calcined samples and those of the corresponding carbon nanocomposites. While the carbon film thickness in C–SBA-15–Ni is about 0.57 nm, the thickness for C–SBA-15#–Ni is estimated as 1.45 nm. Note that the PSD curve for C–SBA-15–Ni shows a maximum at ca. 1.9 nm, although most of the mesopores are located at ca. 7.5 nm. By neglecting any influence caused by Ni during calcinations and by using the pore widths of NiO–SBA-15 and NiO–SBA-15# to estimate the values of the carbon film thickness for C–SBA-15 and C–SBA-15#, the resulting values are found to be 0.45 and 1.07 nm, respectively. Under the assumption that the carbon walls are composed of folded graphene sheets as in CNTs with an average separation of 0.34 nm,[29] the aforementioned values indicate the presence of about 1.5 and 3 graphene sheets in the carbon films formed on the pore walls of SBA-15 and SBA-15#, which is in a good agreement with previous findings.[27,29]

Nitrogen adsorption isotherms for the Ni-containing carbon materials obtained after silica dissolution [see Figure 2(e)] exhibit broader capillary condensation steps, which appear at lower relative pressures than those for the silica nanocomposites. Similar trends are observed for the Ni-free carbon materials, but the adsorption parameters could not be evaluated for MC# because of the small amount of the sample. The data presented in Table 1 reveal that the total pore volume of MC#–Ni is about 55% larger than that for the MC–Ni material. The mesopore widths estimated at the maximum of the PSD curves for the latter materials are about 4–5 nm, i.e. about two times smaller than those for the corresponding Ni-containing SBA-15 samples.

Despite the thicker carbon film in the case of C–SBA-15#, the carbon content in this sample is much lower than that in the C–SBA-15 sample. The carbon content for both samples were obtained from the TG curves in air (see Figure 4). For C–SBA-15, this value is 26.5%, while for C–SBA-15#, the total weight change is 19.3%. The previously reported percentage of carbon deposited within the cylindrical mesopores of SBA-15 is ca. 19%,[29] which corresponds to the carbon amount of a single-walled CNT of ca. 6 nm that coats the siliceous mesopore walls. For a double-walled CNT of ca. 5 nm, the amount of carbon within the cylindrical mesopores of SBA-15 would correspond to ca. 31%. The mesopore width of the C–SBA-15 materials studied are larger than those previously reported.[29] Another interesting feature of the aforementioned carbon materials is a sharp (single) oxidation step at ca. 540 °C, which is similar to the oxidation of graphitic carbon materials.[9] A TG analysis was not performed for the Ni-containing materials because oxidation of the Ni nanoparticles led to a gain in the sample weight, which is in contrast to the carbon weight loss as a result of its oxidation.

The presence of graphitic carbon was further confirmed by the Raman spectra recorded for the Ni-containing materials. As shown in Figure 5, the characteristic bands for amorphous (D band, ≈1300 cm^{-1}) and graphitic carbon ma-

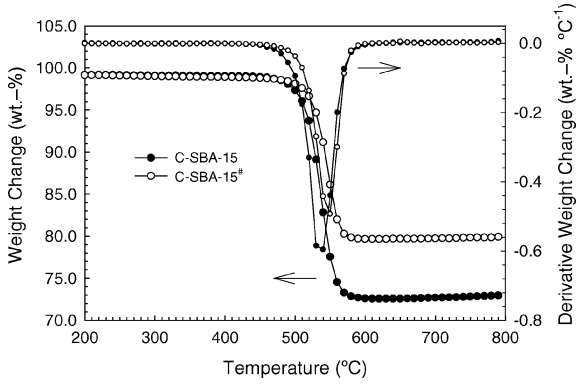

Figure 4. The TG and DTG oxidation profiles for the C–SBA-15 and C–SBA-15$^{\#}$ materials recorded in flowing air.

terials (G band, ≈1600 cm^{-1})[39] could be assigned to the nanocomposites before and after etching of the silica templates. Bands below 900 cm^{-1}, which can be assigned to nickel oxide are visible too.[40] For the template-free materials, the relative intensities of the D and G bands are ca. 0.94, which is comparable to other graphitic carbon materials with amorphous domains.[41] All spectra also show some background contributions from the quartz holder.

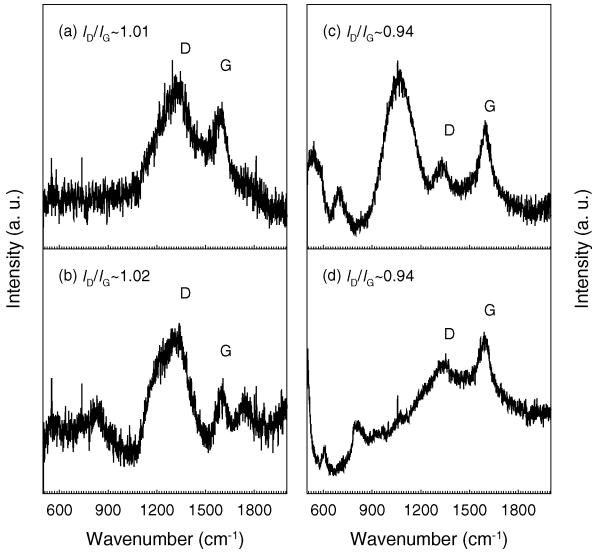

Figure 5. Raman spectra for (a) C–SBA-15–Ni, (b) C–SBA-15$^{\#}$–Ni, and the tubular carbon inverse replicas (c) MC–Ni and (d) MC$^{\#}$–Ni.

The wide angle powder XRD for MC–Ni and MC$^{\#}$–Ni show well-resolved peaks for metallic Ni nanoparticles (see Figure 6). The most intense reflection is located at $2\theta \approx 44°$, which overlaps with peaks for the Al sample holder and possibly carbon. For both materials, the second most-intense reflection for the Ni phase was used to estimate the size of the crystallites by using the Scherer equation, because this reflection is associated only with Ni phase. For both samples, the size of the Ni crystallites is estimated to be ≈60 nm, which does not exclude the existence of nanoparticles of smaller size. Most importantly, the characteristic peak associated with the periodic stacking of graphene layers at about 26° is not observed for both materials. Despite the thickness of the tubular carbon films having about 4 graphene sheets, these films are probably amorphous, although the presence of layered graphene domains may not be excluded.

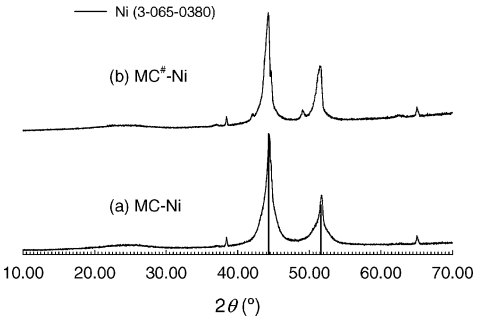

Figure 6. Wide angle powder XRD patterns for (a) MC–Ni and (b) MC$^{\#}$–Ni, and peak assignments for the Ni phase. Peaks for the Al sample holder are present in both patterns.

STEM images of the C–SBA-15–Ni and C–SBA-15$^{\#}$–Ni samples are shown in Figures 7 and 8, respectively. These images reveal a high structural ordering of both carbon-coated SBA-15 samples and confirm the presence of highly dispersed uniform nickel nanoparticles. The in-situ EDX analysis of these particles (see Figure S3 in the Supporting Information) shows a high Ni loading with small amounts of oxygen. Thus, most of the nanoparticles are composed of metallic Ni as evidenced by powder XRD for larger clusters.

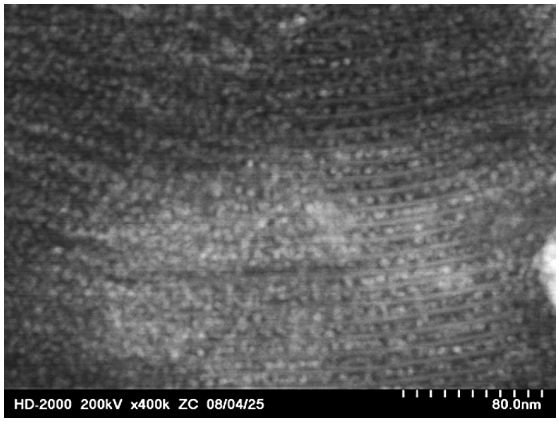

Figure 7. *Z*-contrast TEM image of C–SBA-15–Ni.

For C–SBA-15–Ni (Figure 7), the carbon film deposited on the SBA-15 pore walls is homogeneous, whereas the separation between the Ni nanoparticles within cylindrical mesopores is about 10 to 20 nm. Additional images shown in Figure S4(a) and (b) (Supporting Information) also reveal that the carbon coating and Ni distribution is homogeneous over several hundreds of nanometers along the cylindrical mesopores.

The SEM image of the C–SBA-15$^{\#}$–Ni sample (Figure 8) also reveals a long-range ordering of cylindrical channels along the 110 diffraction plane. The TEM image of the same sample shows a similar uniformity of the carbon film and a homogeneous distribution of the Ni nanoparticles

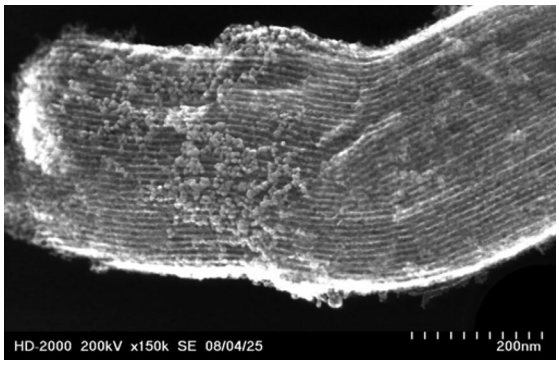

Figure 8. SEM image of C–SBA-15#–Ni.

[Figure S4(c) in the Supporting Information]. Small clusters of nanoparticles are observed on the edges of the carbon–silica particles of C–SBA-15#–Ni, with some larger particles of ca. 60 nm [Figure S4(d) in the Supporting Information].

After removal of the silica template, the MC–Ni and MC#–Ni materials partially retain the inverse replica nanostructure composed of ordered interconnected carbon nanopipes. The STEM images of MC–Ni and MC#–Ni shown in Figures 9 and 10, respectively, reveal that the nickel nanoparticles retain their uniform distribution and size after HF treatment. The *Z*-contrast TEM image in Figure 9 with lower magnification reveals that the particle morphology of MC–Ni is comparable to that of the silica nanocomposites [see also Figure S5 in the Supporting Information]. Both images also confirm that the Ni nanoparticles are widely spread throughout the whole sample and within the tubular carbon channels.

The images of MC#–Ni indicate the presence of some carbon tubes with additional Ni nanoparticles on the external surface. The SEM image of the same sample at lower magnification (Figure S5 in the Supporting Information) shows the ordered tubular nanostructures with a length of several hundreds of nanometers. The *Z*-contrast TEM analysis confirms wide dispersion of the Ni nanoparticles within the MC#–Ni channels, similar to that for MC–Ni.

The mechanism of graphitization in the presence of Ni catalysts has been the subject of debate for a long time. A simple model has been proposed on the basis of a series of TEM images taken at different stages of thermal treatment of the nickel–amorphous-carbon thin films.[42] According to this study, the Ni nanoparticles formed on the surface of the carbon films, have a protective graphitic shell. The pressure created by the carbon shell expels Ni from its interior, which continues to migrate on the amorphous film surface. Furthermore, the presence of graphitic domains is found to halt the migration of such nanoparticles; however, in none of these steps is the presence of carbide phases detected.

With regard to the samples studied here, such small nanoparticles could be formed within carbon-coated mesopore channels, but their migration is limited because of the presence of small graphitic domains left by other particles. As a result of the aforementioned space limitation, the nickel nanoparticles formed within mesopore channels look like "peapod-type" structures (see Figure 7). The particles formed near the edges of the carbon-coated silica particles

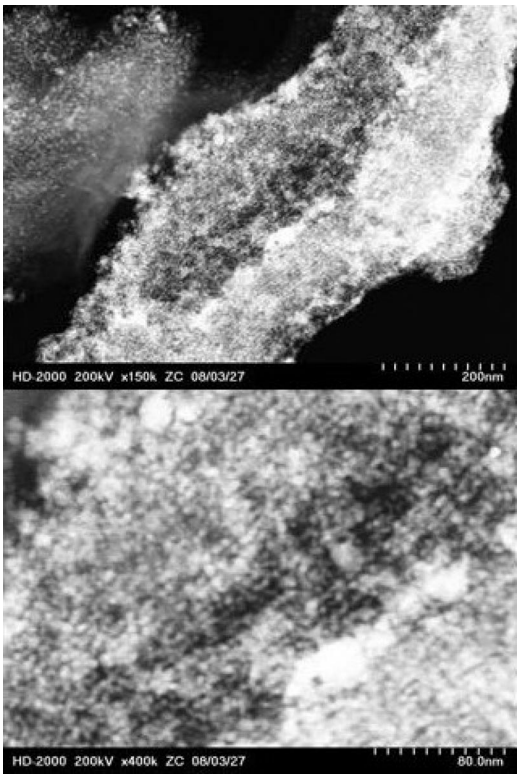

Figure 9. *Z*-contrast TEM images of MC–Ni at lower (top) and higher magnifications (bottom) of the same sample.

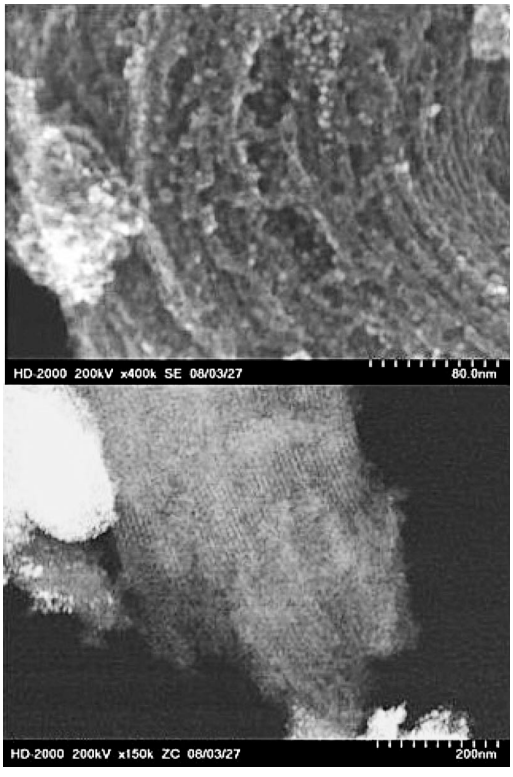

Figure 10. SEM (top) and *Z*-contrast TEM (bottom) images of MC#–Ni.

are able to diffuse and coalesce with other Ni nanoparticles to form larger clusters with a size of at least 60 nm. Further, partial collapse of the carbon nanostructures consisting of ultra thin-walled pipes could facilitate a release of additional Ni nanoparticles to form the aforementioned clusters. A similar distribution of metallic Ni has been reported for the synthesis of multiwalled CNTs in the presence of Ni catalyst and single-walled CNTs,[32] whereas somewhat different results have been obtained in the case of CMK-3, which consists of interconnected carbon nanorods.[17–19]

Conclusions

Mesoporous carbon materials with ultra-thin walls have been successfully prepared by using SBA-15 silica as hard templates and 2,3-di-hydroxynaphthalene as a carbon precursor. Addition of a concentrated 2-propanol solution of $Ni(NO_3)_2{\cdot}6H_2O$ to the SBA-15–carbon nanocomposites followed by thermal treatment at about ca. 800 °C resulted in partially graphitic carbon materials containing uniformly dispersed metallic Ni nanoparticles with traces of NiO. Furthermore, the formation of Ni nanoparticles in the channels of the aforementioned composites afforded stable Ni-containing "peapod-type" ordered nanostructures with small graphitic domains. The mechanism of formation of the aforementioned materials seems to be analogous to the recently proposed model for the behavior of Ni on amorphous carbon films.[42] Further, a similar distribution of Ni nanoparticles was observed during the synthesis of multiwalled CNTs in the presence of Ni catalysts.[32] Previous reports on the synthesis of CMK-3 carbon materials[17–19] indicated that larger NiO particles are embedded within the carbon frameworks. In comparison with the aforementioned Ni-containing CMK-3 and CNT materials, the carbon materials reported in this work exhibit highly dispersed and uniform Ni nanoparticles, in addition to high surface area, large pore volume, and consequently, better pore accessibility, which make them promising materials for applications in catalysis and energy-related applications.

Experimental Section

Synthesis of SBA-15 and Nickel-Containing Nanocomposites and Carbon Materials: For the synthesis of SBA-15, poly(ethylene oxide)–poly(propylene oxide)–poly(ethylene oxide) triblock copolymer (4.00 g, PEO_{20}–PPO_{70}–PEO_{20}; Pluronic 123 from BASF) was added to an aqueous solution of hydrochloric acid (144 mL of a 1.7 M solution) and stirred for 4 h at 40 °C. Tetraethylorthosilicate (TEOS, Fluka) was then added dropwise (mass ratio of TEOS/P123 = 2), and the polymer/TEOS synthesis mixture was stirred for 2 or 6 h. The synthesis gels were transferred to Teflon-lined sealed containers, and the gel stirred for 2 h was kept at 100 °C for 48 h, whereas the gel stirred for 6 h was kept at 140 °C for 24 h under static conditions. The final products were filtered, washed with water, and dried for 12 h at 80 °C. Both polymer-containing silica samples were calcined at 540 °C for 3 h under flowing air with a heating rate of 5 °C min^{-1}. The samples obtained at 100 and 140 °C were labeled as SBA-15 and SBA-15$^{\#}$, respectively, where # refers to the hydrothermal treatment temperature of 140 °C.

The carbon–SBA-15 and carbon inverse replicas were prepared according to a slightly modified procedure proposed by Nishihara et al.[29] 2,3-dihydroxynaphthalene (approximately 3.00 g, DHN, 98%, Acrós) was dissolved in acetone (50.00 mL, Acrós). To the DHN solution, SBA-15 (≈0.5 g) was added, and the sol stirred for 20 h at room temperature. The solvent was then evaporated under vacuum and heating (≈80 °C water bath), and the mixture was dried overnight at ≈80 °C. The resulting solids were thermally treated in flowing N_2 at 300 °C for 2 h and with a 1 °C min^{-1} heating rate. The thermal treatment was repeated twice for each sample. The obtained powders were then filtered and washed with excess acetone, and the recovered solids dried at 80 °C overnight under vacuum and labeled DHN–SBA-15 and DHN–SBA-15$^{\#}$. These samples were thermally treated at 800 °C in flowing N_2 for 4 h and with a heating rate of 3 °C min^{-1}, and the final carbon–SBA-15 nanocomposites were labeled as C–SBA-15 and C–SBA-15$^{\#}$.

For the materials containing nickel, nickel nitrate (≈2.87 g, $Ni(NO_3)_2{\cdot}6H_2O$, Acrós) was dissolved in 2-propanol (50.00 mL, Acrós Organics) and then quickly mixed with DHN-SBA-15 or DHN-SBA-15$^{\#}$ (≈1.0 g) containing the carbonaceous precursor, and dried at 80 °C. The latter was then thermally treated under the same conditions used in the preparation of the nickel-free nanocomposites. The resulting samples were labeled as C–SBA-15–Ni and C–SBA-15$^{\#}$–Ni. The silica in all nanocomposites was removed using HF (Acrós Organics) solution for 24 h at room temperature, filtered, washed with water, and vacuum dried at 80 °C overnight. The resulting carbon materials were denoted as MC and MC$^{\#}$, whereas the Ni-containing carbon materials were denoted as MC–Ni and MC$^{\#}$–Ni, respectively. The NiO–SBA-15 and NiO–SBA-15$^{\#}$ samples were obtained by calcination of the corresponding C–SBA-15–Ni and C–SBA-15$^{\#}$–Ni, respectively, in flowing air at 500 °C.

Characterization: The calcined SBA-15, carbon–silica nanocomposites, and carbon replicas were characterized by thermogravimetric analysis (TG), nitrogen adsorption at –196 °C, powder X-ray diffraction, Raman spectroscopy, and transmission electron microscopy (TEM). The TG measurements for as-synthesized silica–triblock-copolymer composites and related carbon materials were performed by using the high resolution mode of a TA Instruments TGA 2950 thermogravimetric analyzer. The TG profiles were recorded up to 800 °C in flowing air, with a heating rate of 10 °C min^{-1}. Nitrogen adsorption isotherms were measured at –196 °C with ASAP 2010 and 2020 volumetric adsorption analyzers manufactured by Micromeritics (Norcross, GA). Before adsorption measurements, the silica, carbon–silica and carbon samples were outgassed under vacuum for at least 2 h at 200 °C. The specific surface area of the samples was calculated by using the BET method within the relative pressure range of 0.05 to 0.2.[43] The PSDs were determined by using the BJH method calibrated for cylindrical pores according to the improved KJS method.[44] Small and wide angle XRD patterns were recorded on a PANanalytical Inc., X′Pert Pro (MPD) Multi Purpose Diffractometer with Cu-K_α radiation (0.1540 nm), an operating voltage of 40 kV and 40 mA, 0.01° step size, and 20 s step time for small angle measurements ($0.40° < 2\theta < 5.00°$) and 0.02° step size (6 s step time) for wide angle measurements ($5.00° < 2\theta < 70.00°$). Microscope glass slides were used as sample holders for small and wide angle measurements for the silica–carbon composites, whereas standard Al holders (PANanalytical PW1172, 15 × 20 × 1.8 mm) were used for wide angle measurements for the final carbon replicas. The samples were manually ground prior to XRD analysis, and all measurements were performed at room temperature. Crystallite dimensions (D) of the nickel species were estimated with the Scherrer equation D =

$0.90\lambda/\beta\cos\theta$, where 0.90 is a constant, λ is 0.1540 nm; β is the full width at half maximum of the peak at the diffraction angle θ. Raman spectra were recorded with a HORIBA Jobin Yvon HR800 with a microscope attachment. The laser wavelength of 633 nm was focused using a diffraction limited spot, and the scan time was 2 s for each sample. For the STEM analysis, the sample powders were dispersed in ethanol by moderate sonication at concentrations of 5 wt.-% of the solids. A Lacy carbon-coated 200-mesh copper TEM grid was first dipped into the sample suspension and then dried under vacuum at 80 °C for 12 h prior to microscopic analysis. All samples were imaged by a Hitachi HD-2000 Scanning and Transmission Electron Microscope (STEM). The unit was operated at an acceleration voltage of 200 kV and an emission current of 30 mA. The samples were imaged by a secondary electron detector, an annular disk *Z*-contrast detector, and a transmission electron detector. The same sample spots were used to simultaneously take SEM, *Z*-contrast (dark-field images), and TEM images. The energy dispersive X-ray spectra (EDX) were collected by a detector controlled through another computer that acquired signals from the selected area of the samples. The EDX spectra were collected at 30% of the detector dead-time and 3 min of the acquisition time.

Supporting Information (see footnote on the first page of this article): Small angle XRD spectra, nitrogen adsorption isotherms at –196 °C, and the corresponding PSDs for C–SBA-15, C–SBA-15$^{\#}$, MC and MC$^{\#}$, EDX spectra for MC–Ni and MC$^{\#}$–Ni, STEM and *Z*-contrast TEM images for C–SBA-15–Ni, C–SBA-15$^{\#}$–Ni, MC–Ni, and MC$^{\#}$–Ni are presented.

Acknowledgments

The authors thank BASF for providing the triblock polymer. The STEM characterization of the samples studied was conducted at the Center for Nanophase Materials Sciences, which is sponsored by the Oak Ridge National Laboratory, Division of Scientific User Facilities, U. S. Department of Energy.

[1] J. S. Beck, J. C. Vartuli, W. J. Roth, M. E. Leonowicz, C. T. Kresge, K. D. Schimitt, C. T.-W. Chu, D. H. Olson, E. W. Sheppard, S. B. McCullen, J. B. Higgins, J. L. Schlenker, *J. Am. Chem. Soc.* **1992**, *114*, 10834–10843.
[2] D. Zhao, J. Feng, Q. Huo, N. Melosh, G. H. Fredrickson, B. F. Chmelka, G. D. Stucky, *Science* **1998**, *279*, 548–552.
[3] S. Jun, S. H. Joo, R. Ryoo, M. Kruk, M. Jaroniec, Z. Liu, T. Ohsuna, O. Terasaki, *J. Am. Chem. Soc.* **2000**, *122*, 10712–10713.
[4] S. H. Joo, S. J. Choi, I. Oh, J. Kwak, Z. Liu, O. Terasaki, R. Ryoo, *Nature* **2001**, *412*, 169–172.
[5] M. Kruk, M. Jaroniec, T.-W. Kim, R. Ryoo, *Chem. Mater.* **2003**, *15*, 2015–2823.
[6] M. Kruk, M. Jaroniec, C. H. Ko, R. Ryoo, *Chem. Mater.* **2000**, *12*, 1961–1968.
[7] R. Ryoo, S. H. Joo, S. Jun, *J. Phys. Chem. B* **1999**, *103*, 7743–7746.
[8] T.-W. Kim, R. Ryoo, K. P. Gierszal, M. Jaroniec, L. A. Solovyov, Y. Sakamoto, O. Terasaki, *J. Mater. Chem.* **2005**, *15*, 1560–1571.
[9] T.-W. Kim, I.-S. Park, R. Ryoo, *Angew. Chem. Int. Ed.* **2003**, *42*, 4375–4379.
[10] Y. Xia, R. Mokaya, *Adv. Mater.* **2004**, *16*, 1553–1558.
[11] A. B. Fuertes, *J. Mater. Chem.* **2003**, *13*, 3085–3088.
[12] Y. Xia, Z. Yang, R. Mokaya, *Chem. Mater.* **2006**, *18*, 1141–1148.
[13] J. Fan, T. Wang, C. Yu, B. Tu, Z. Jiang, D. Zhao, *Adv. Mater.* **2004**, *16*, 1432–1436.
[14] S. Zhu, H. Zhou, M. Hibino, I. Honma, M. Ichihara, *Adv. Funct. Mater.* **2005**, *15*, 381–386.
[15] C. Minchev, H. Huwe, T. Tsoncheva, D. Paneva, M. Dimitrov, I. Mitov, M. Fröba, *Microporous Mesoporous Mater.* **2005**, *81*, 333–341.
[16] H. Huwe, M. Fröba, *Carbon* **2007**, *45*, 304–314.
[17] Y. Cao, J. Cao, M. Zheng, J. Liu, G. Ji, *J. of Solid State Chem.* **2007**, *180*, 792–798.
[18] H. Li, S. Zhu, H. Xi, R. Wang, *Microporous Mesoporous Mater.* **2006**, *60*, 943–946.
[19] H. Li, H. Xi, S. Zhu, R. Wang, *Mater. Lett.* **2006**, *179*, 91–95.
[20] I. Grigoriants, L. Sominski, H. Li, I. Ifargan, D. Aurbach, A. Gedanken, *Chem. Commun.* **2005**, 921–923.
[21] J. Lee, S. Jin, Y. Hwang, J.-G. Park, H. M. Park, T. Hyeon, *Carbon* **2005**, *43*, 2536–2543.
[22] J. Ding, K.-Y. Chan, J. Ren, J. Xiao, *Electrochim. Acta* **2005**, *50*, 3131–3141.
[23] M.-L. Lin, C.-C. Huang, M.-Y. Lo, C.-Y. Mou, *J. Phys. Chem. C* **2008**, *112*, 867–873.
[24] A.-H. Lu, W.-C. Li, W. Schmidt, W. Kiefer, F. Schüth, *Carbon* **2004**, *42*, 2939–2948.
[25] I. S. Park, M. Choi, T.-W. Kim, R. Ryoo, *J. Mater. Chem.* **2006**, *16*, 3409–3416.
[26] Z. Lei, S. Bai, Y. Xiao, L. Dang, L. An, G. Zhang, Q. Xu, *J. Phys. Chem. C* **2008**, *112*, 722–731.
[27] A. Y. Lo, S. J. Huang, W. H. Chen, Y. R. Peng, C. T. Kuo, S. B. Liu, *Thin Solid Films* **2006**, *498*, 193–197.
[28] K. P. Gierszal, M. Jaroniec, *J. Am. Chem. Soc.* **2006**, *128*, 10026–10027.
[29] H. Nishihara, Y. Fukura, K. Inde, K. Tsuji, M. Takeuchi, T. Kyotani, *Carbon* **2008**, *46*, 48–53.
[30] K. Kamegawa, H. Yoshida, *J. Colloid Interf. Sci.* **1993**, *159*, 324–327.
[31] K. Kamegawa, H. Yoshida, *Carbon* **1997**, *35*, 631–639.
[32] J. Cheng, X. Zang, Y. Ye, *J. Solid State Chem.* **2006**, *179*, 91–95.
[33] G.-h. Yuan, Z.-h. Jiang, A. Aramata, Y.-z. Gao, *Carbon* **2005**, *43*, 2913–2917.
[34] I. Hotovy, V. Rehacek, P. Siciliano, S. Capone, L. Spiess, *Thin Solid Films* **2002**, *418*, 9–15.
[35] R. Qiu, X. L. Zhang, R. Qiao, Y. Li, Y. I. Kim, Y. S. Kang, *Chem. Mater.* **2007**, *19*, 4174–4180.
[36] C. Xu, Y. Hu, J. Rong, S. P. Jiang, Y. Lui, *Electrochem. Commun.* **2007**, *9*, 2009–2012.
[37] G. P. Jin, Y.-F. Ding, P.-P. Zheng, *J. Power Sources* **2007**, *166*, 80–86.
[38] J. Gorka, M. Jaroniec in *Nanoporous Materials* (Eds.: A. Sayari, M. Jaroniec), World Scientific Publishing Co., Singapore, **2008**, pp. 333–346.
[39] P. K. Chu, L. Li, *Mater. Chem. Phys.* **2006**, *96*, 253–277.
[40] C. Xu, G. Xu, G. Wang, *J. Mater. Science* **2002**, *38*, 779–782.
[41] A. B. Fuertes, T. A. Centeno, *J. Mater. Chem.* **2005**, *15*, 1079–1083.
[42] R. Anton, *Carbon* **2008**, *46*, 656–662.
[43] M. Kruk, M. Jaroniec, *Chem. Mater.* **2001**, *13*, 3169–3183.
[44] M. Jaroniec, L. A. Solovyov, *Langmuir* **2006**, *22*, 6757–6760.

Received: July 7, 2008
Published Online: January 8, 2009

